

See discussions, stats, and author profiles for this publication at: <https://www.researchgate.net/publication/267041133>

# Colloidal Indium-Doped Zinc Oxide Nanocrystals with Tunable Work Function: Rational Synthesis and Optoelectronic Applications

ARTICLE in CHEMISTRY OF MATERIALS · AUGUST 2014

Impact Factor: 8.35 · DOI: 10.1021/cm502812c

---

CITATIONS

10

---

READS

37

## 13 AUTHORS, INCLUDING:



Sai Bai

University of Oxford, Linköping University

17 PUBLICATIONS 141 CITATIONS

[SEE PROFILE](#)



Dai Xingliang

Zhejiang University

6 PUBLICATIONS 99 CITATIONS

[SEE PROFILE](#)



Haiping He

Zhejiang University

181 PUBLICATIONS 2,677 CITATIONS

[SEE PROFILE](#)



Jianpu Wang

Nanjing Tech University

36 PUBLICATIONS 805 CITATIONS

[SEE PROFILE](#)

# Colloidal Indium-Doped Zinc Oxide Nanocrystals with Tunable Work Function: Rational Synthesis and Optoelectronic Applications

Xiaoyong Liang,<sup>†</sup> Yuping Ren,<sup>†</sup> Sai Bai,<sup>†</sup> Na Zhang,<sup>†</sup> Xingliang Dai,<sup>†</sup> Xin Wang,<sup>†</sup> Haiping He,<sup>†</sup> Chuanhong Jin,<sup>†</sup> Zhizhen Ye,<sup>†</sup> Qi Chen,<sup>‡</sup> Liwei Chen,<sup>‡</sup> Jianpu Wang,<sup>†,§</sup> and Yizheng Jin<sup>\*,†,||</sup>

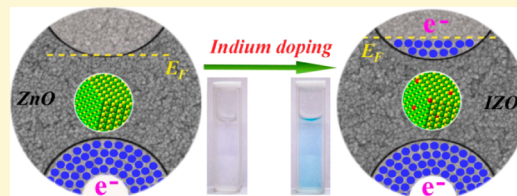
<sup>†</sup>State Key Laboratory of Silicon Materials, Cyrus Tang Center for Sensor Materials and Applications, Department of Materials Science and Engineering, and <sup>||</sup>Center for Chemistry of High-Performance and Novel Materials, Zhejiang University, Hangzhou 310027, People's Republic of China

<sup>‡</sup>Suzhou Institute of Nano-Tech and Nano-Bionics, Chinese Academy of Sciences, 398 Ruoshui Road, Suzhou Industrial Park, Suzhou 215123, P. R. China

<sup>§</sup>Institute of Advanced Materials, Nanjing Tech University, Nanjing 210009, China

## Supporting Information

**ABSTRACT:** Transition metal oxides are widely used in solution-processed optoelectronic devices as charge-transporting interlayers to improve contact properties and device performances. Here we show that the work function of oxide nanocrystal thin films, one of the most important parameters for charge-transporting interlayers, is readily tuned by rational design of material synthesis. Mechanism studies reveal that the combination of employing the reverse-injection approach and using zinc stearate and indium 2-ethylhexanoate as the cationic precursors ensures both controlled reaction pathways and balanced relative dopant-host precursor reactivity and hence high-quality indium doped zinc oxide nanocrystals. We find that the empirical rule of relative Lewis acidity fails to predict the relative reactivity of the cationic precursors and quantitative measurements are obligatory. The successful incorporation of indium dopants into host oxide nanocrystals accompanied by the generation of high density of free electrons leads to oxide thin films with lower work function. Polymer light-emitting diodes with electron-transporting interlayers based on the indium doped zinc oxide nanocrystals exhibit improved electron-injection properties and enhanced device characteristics, i.e., lower turn-on voltage, higher maximum luminance, and higher efficiency. Our study is an excellent example that new understanding on the chemical kinetics of doped nanocrystals leads to rational design of synthetic protocols and materials with tailored electronic properties, providing benefits for their optoelectronic applications.



## INTRODUCTION

Solution-processed optoelectronic devices promise low fabrication cost, large device area, and physical flexibility by employing high-throughput printing and coating techniques.<sup>1–3</sup> Colloidal semiconductor nanocrystals, which offer both solid-state properties and solution processability, are attractive building blocks for solution-processed optoelectronics devices.<sup>4–9</sup>

Recently, transition metal oxide thin films were utilized as charge-transporting interlayers (CTLs) in solution-processed optoelectronic devices to improve contact properties, leading to devices with efficient charge extraction/injection characteristics and enhanced stability.<sup>10–16</sup> For metal oxide CTLs, work function is one of the most important parameters. The work function of oxide CTLs and the electronic structures of the contacting layers govern the interfacial energy-level alignment and hence the charge injection/extraction barriers.<sup>17,18</sup> The work function of oxide CTLs influences the built-in field and thus affects important physical processes, such as charge transport and recombination, in the active layers.<sup>16,19</sup> There-

fore, controlling the work function of oxide CTLs is critical for achieving high-performance optoelectronic devices.

Employment of colloidal oxide nanocrystals, which decouples the oxide-synthesis step from the film-deposition step, is an attractive strategy to fabricate oxide CTLs.<sup>20–24</sup> Owing to the excellent solution dispersibility, colloidal oxide nanocrystals can be readily integrated into devices by a variety of solution-based techniques. In addition, it is possible to tailor the properties of oxide nanocrystals via rational design of material synthesis.<sup>25–29</sup>

We propose that rational synthesis of doped oxide nanocrystals provides an effective strategy to control the work function of CTLs based on colloidal oxide nanocrystals. Work function of a material has two contributions: electron chemical potential, i.e., Fermi level relative to the absolute vacuum level, and surface dipole.<sup>30</sup> A few techniques, such as employment of self-assembled monolayers, were utilized to change the work function of oxide thin films via altering the surface dipoles.<sup>31</sup> In contrast, the electron chemical potential of a metal oxide is

Received: July 30, 2014

Published: August 7, 2014

more associated with its intrinsic properties. For binary oxides, defects, such as oxygen vacancies and interstitials or cation vacancies and interstitials, are known to affect the work function.<sup>18,32</sup> Introduction of specific dopant ions into oxide semiconductors also changes their work function. For instance, n-type dopants raise the Fermi level, thus reducing the work function. From material characterization standpoint, controlled doping of colloidal oxide nanocrystals is more straightforward than the approach of defect engineering. In this study, we adopt the strategy of controlled doping to alter the electronic properties of oxide nanocrystals. Note that for a few colloidal oxide nanocrystal systems, doping has been demonstrated to be an effective way for controlling the carrier concentrations.<sup>25,29,33–35</sup> However, to the best of our knowledge, there is no report in the literature on modulation of the work function of oxide CTLs by rational synthesis of doped oxide nanocrystals.

A second scope of this contribution is to study the chemical reactions, i.e. precursor conversion pathways and chemical kinetics, involved in the formation of colloidal doped oxide nanocrystals. As shown by many reports on the chemical reactions associated with the syntheses of quantum dots, such as CdSe, CdS and InP nanocrystals,<sup>36–39</sup> precursor conversion is the rate-limiting step. The size, size distribution and shape of the semiconducting nanocrystals are largely controlled by the reactivity of precursors.<sup>40–42</sup> Regarding doped nanocrystals, there have been many mechanism studies that investigated their crystallization processes and the interactions between dopant ions and host lattices.<sup>27,43–45</sup> However, knowledge on the relationship between chemical reactions and formation of colloidal doped nanocrystals is still limited. This situation may be partly due to that doping adds another dimension of difficulty in analyzing the chemical reactions of precursors. Reaction pathways of either dopant precursor or host precursor may be different from what are originally hypothesized. Furthermore, for doped oxide nanocrystal systems, there is a lack of quantitative studies on chemical kinetics of precursor conversion reactions.

Herein, colloidal indium-doped ZnO (IZO) nanocrystals are used as a model system to study the doping effects on the work function of the oxide electron-transporting interlayers (ETLs). Zinc oxide (ZnO) is one of the most promising materials for ETL applications because of the unique combination of low work function, excellent optical transparency, high electron mobility, hole-blocking properties, and environmentally friendly nature. ETLs based on colloidal ZnO nanocrystals have been integrated into a range of solution-processed devices including polymer light emitting diodes (PLEDs), bulk heterojunction organic photovoltaics, quantum dot light emitting diodes and hybrid perovskite solar cells.<sup>21,46–48</sup> Indium, a group III element acting as n-type dopant for ZnO, may raise the Fermi level of the oxide nanocrystals, thus influencing the work function of thin films based on doped oxide nanocrystals. To this end, we study controlled synthesis of colloidal IZO nanocrystals. The temperature-dependent reaction pathways and the reactivity of different cationic precursors were investigated by Fourier transform infrared spectroscopy (FTIR). The resulting understanding allowed us to rationally design the synthetic procedures and select suitable cationic precursors, leading to controlled doping for quality colloidal oxide nanocrystals. The IZO nanocrystals were applied in PLED as ETLs, revealing the impact of indium doping on the contact properties and device performances.

## ■ EXPERIMENTAL SECTION

**Materials.** Indium nitrate ( $\text{In}(\text{NO}_3)_3$ ), 2-ethylhexanoic acid, tetramethylammonium hydroxide entahydrate (TMAH), zinc stearate ( $\text{Zn}(\text{St})_2$ ), zinc 2-ethylhexanoate ( $\text{Zn}(\text{EH})_2$ ), and 1-octadecanol (ODA) were purchased from Alfa Aesar. 1-octadecene (ODE) and hexylamine were purchased from Acros Organics. Stearic acid (HSt) was purchased from Sigma-Aldrich. All chemicals were used as received.

**Synthesis of IZO Nanocrystals.** Two approaches, namely the injection approach and the reverse-injection approach, were used. The injection approach is similar to the previous synthetic protocol for the growth of Mg-doped ZnO nanocrystals.<sup>27</sup> In a typical reaction, 0.6 mmol of metal precursors and 12 g of ODE were loaded into a 50 mL three-necked flask. The flask was purged with argon, and then degassed under vacuum at 100 °C for 30 min. Next the solution was heated to 270 °C under an argon flow. A separate solution of 6 mmol of ODA in ODE (6 g) which was also degassed and heated to 180 °C was swiftly injected into the reaction flask. The reaction temperature dropped to ~250 °C and was kept at this temperature for 60 min. The resulting nanocrystals were precipitated by a mixture of ethanol and ethyl acetate, collected by centrifugation, and then carefully purified with hexane/ethanol mixtures. In the reverse-injection approach, ODA (6 mmol) and ODE (13.5 g) were loaded into a reaction flask, degassed and then heated to 270 °C. A separate ODE solution containing the metal precursors was degassed at 100 °C, heated to 150 °C and then injected into the alcohol solution to initial the alcoholysis reaction at 250 °C. A set of parallel reactions, namely pure ZnO reactions, 0.5, 1.0, 1.3, 1.5, 1.8, 2.0, 3.0, 5.0, 10, and 20 mol % indium 2-ethylhexanoate ( $\text{In}(\text{EH})_3$ ) reactions and pure  $\text{In}_2\text{O}_3$  reactions were carried out. For example, in a 10 mol %  $\text{In}(\text{EH})_3$  reaction, 0.06 mmol of  $\text{In}(\text{EH})_3$  and 0.54 mmol of  $\text{Zn}(\text{St})_2$  were used as the cationic precursors.

When indium stearate ( $\text{In}(\text{St})_3$ ) and  $\text{Zn}(\text{St})_2$  were used as the cationic precursors, the flask containing the precursor solution was kept at 120 °C before injecting into ODA solution (275 °C) to avoid the hydrolysis of  $\text{In}(\text{St})_3$ .

**Measuring the Initial Reaction Rates of the Alcoholysis Reactions.** The alcoholysis reactions of different metal precursors were monitored by FTIR. Aliquots (0.3  $\mu\text{L}$ ) taken by microsyringes at different time intervals were spread onto  $\text{CaF}_2$  substrates to form smooth films with even thickness. Note that the thickness of the films was optimized so that the absorbance peaks were reasonably strong to maximize the signal-to-noise ratio and did not exceed the linear range of the instrument. These samples were used for FTIR analyses. The concentration of ester was calculated by integrating peak area using the  $\text{C}=\text{C}$  vibration band of ODE at  $1641 \text{ cm}^{-1}$  as the reference. The resulting curves of ester concentration V.S. reaction time were fitted by exponential function because the concentration of alcohol was treated as constant within the time of measurements and the reaction order for metal carboxylate salts was determined to be close to 1.<sup>53</sup> The values of initial reaction rates were obtained by extracting the slopes of the fitted curves at  $t = 0$ .

**Ligand Exchange of Oxide Nanocrystals.** When the alcoholysis reaction was finished, the reaction solution was cooled to 120 °C. In situ ligand-exchange processes were conducted by introducing 5 mL of hexylamine into the flask. The mixture was stirring overnight at 120 °C. The resulting nanocrystals were precipitated by a mixture of ethanol and ethyl acetate, collected by centrifugation, and further purified with hexane/ethanol mixtures. The ligand-exchanged oxide nanocrystals were dispersed in chloroform and used for the fabrication of thin films.

**Oxide Nanocrystal Thin Films.** were deposited onto ITO-glass substrates. The substrates were cleaned by ultrasonication in acetone, deionized water and isopropyl alcohol for 20 min, respectively, followed by oxygen-plasma treatment for 10 min. Then the oxide nanocrystal solutions (~30 mg/mL) were deposited by spin-coating at 3000 rpm, followed by annealing at 140 °C for 40 min in a nitrogen filled glovebox.

**PLED Devices.** were fabricated by spin-coating an m-xylene solution of Poly(9,9-diptylfluorene-*alt*-benzothiadiazole) (F8BT) (14 mg/mL) onto oxide nanocrystal coated ITO-glass substrates to obtain thin films with a thickness of ~100 nm. Bilayer top electrodes of  $M_oO_x/Al$  (10/100 nm) were deposited by thermal evaporation under a base pressure of  $6 \times 10^{-7}$  Torr. The device area was 3.24 mm<sup>2</sup> defined by the overlapping of the ITO and top electrodes. For the PLED characterizations, we used a Keithley 2400 electrometer for electrical measurements and a fiber integration sphere (FOIS-1) coupled with a QE-6500 spectrometer for light-output measurements.<sup>14</sup>

Details of characterization techniques and syntheses of indium precursors are provided in the Supporting Information.

## RESULTS AND DISCUSSION

**Controlling the Reaction Pathways and Balancing the Relative Reactivity of Cationic Precursors.** Our doping strategy is based on alcoholysis of both zinc carboxylate salt and indium carboxylate salt in a noncoordination solvent, ODE, at elevated temperatures. Our initial attempts of activating the metal precursors,  $Zn(St)_2$  and  $In(St)_3$  (see Figure S1a in the Supporting Information) by injection of alcohol at high reaction temperatures to generate single-phase IZO nanocrystals were not successful.<sup>49</sup> A few individual nanocrystals with cubic structures matching corundum-type  $In_2O_3$  were observed in HRTEM analyses (see Figure S2 in the Supporting Information).

We hypothesize that the failure to synthesize phase-pure IZO nanocrystals is due to an unintentional reaction pathway, the hydrolysis of  $In(St)_3$  at elevated temperature.<sup>50</sup> FTIR technique was used to reveal the molecular mechanisms associated with the formation of oxide nanocrystals.<sup>27,28,50–52</sup> Therefore, the temperature-dependent FTIR spectra of the metal precursors in ODE were recorded to determine the reaction pathways. As shown in Figure 1a, when the temperature reached 160 °C, the presence carbonyl absorption of carboxylic acid groups at the peak of ~1710 cm<sup>-1</sup> indicated that hydrolysis reactions occurred. In contrast, hydrolysis of  $Zn(St)_2$  was not evident at temperatures as high as 220 °C (Figure 1b). These results suggest that in the process of heating the cationic precursors to the high reaction temperature of 270 °C, the hydrolysis of  $In(St)_3$  took place and thereby oxide nanocrystals having cubic structures was generated.

A reverse-injection approach was designed to suppress the undesirable hydrolysis reactions.<sup>28</sup> Hydrolysis of metal carboxylates is endothermic. Lower temperatures hinder the hydrolysis reactions. Therefore, in the reverse-injection approach, the solution containing  $Zn(St)_2$  and  $In(St)_3$  was degassed and kept at 120 °C before the injection into the reaction flask heated to 275 °C to initiate the alcoholysis processes. Nevertheless, the reverse-injection approach still does not yield phase-pure IZO nanocrystals. As shown in Figure S3 in the Supporting Information, nanocrystals with cubic structures matching corundum-type  $In_2O_3$  were found in HRTEM analyses.

We further hypothesize that in the reverse-injection approach, the formation of nanocrystals with cubic structures may be due to the unbalanced reactivity of the cationic precursors. To test this hypothesis, we used our recently developed method based on FTIR to accurately measure the initial reaction rates of the alcoholysis reactions.<sup>53</sup> The reverse-injection alcoholysis reactions starting with 0.6 mmol of  $Zn(St)_2$  or 0.4 mmol of  $In(St)_3$  were conducted under identical conditions. As shown in Figure 2a, b, the initial ester-formation

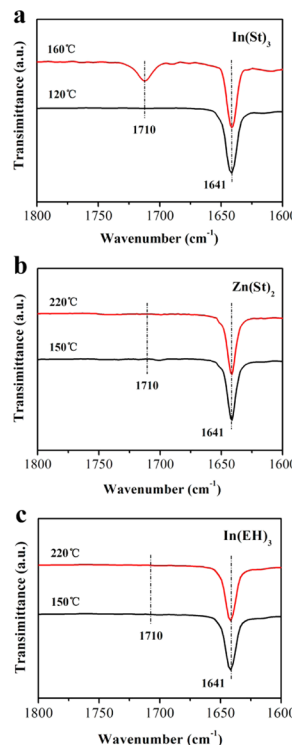


**Figure 1.** Temperature-dependent FTIR spectra of (a)  $In(St)_3$  (0.4 mmol) dissolved in ODE (3 g) at 120 and 160 °C, (b)  $Zn(St)_2$  (0.6 mmol) dissolved in ODE (3 g) at 150 and 220 °C and (c)  $In(EH)_3$  (0.4 mmol) at 150 and 220 °C, respectively. The mixtures were degassed multiple times at 100 °C. All spectra are normalized to the relatively intense C=C vibration band at 1641 cm<sup>-1</sup> originating from ODE.

rates for the reactions using  $Zn(St)_2$  and  $In(St)_3$  as precursors are 11 and 42 mmol L<sup>-1</sup> min<sup>-1</sup>, respectively. These values show that  $In(St)_3$  is much more reactive than  $Zn(St)_2$ .

From the view of chemical kinetics, a key concept linking the chemical reactions and the crystallization processes of doped nanocrystals is that adequate host crystal growth and dopant incorporation rates rely on a balanced host-dopant precursor reactivity.<sup>29,54</sup> In our case,  $In(St)_3$  is far more reactive than  $Zn(St)_2$ . The unbalanced host-dopant precursor reactivity causes segregation of dopant nanophases rather than formation of IZO nanocrystals.

We use  $In(EH)_3$  (see Figure S1b in the Supporting Information) to replace  $In(St)_3$ , aiming to lower the reactivity of the indium precursor. As shown in Figure 2c, the ester formation rate for the reactions starting with 0.4 mmol of  $In(EH)_3$  is 10 mmol L<sup>-1</sup> min<sup>-1</sup>, much lower than that for the reactions starting with 0.4 mmol of  $In(St)_3$  and close to that for the reactions starting with 0.6 mmol of  $Zn(St)_2$ . The different reactivity of the indium precursors comes from the molecular structure of the carboxylate ions. The 2-ethylhexanoate ion has a side-chain structure while the stearate ion has a linear structure. Therefore, when the indium precursors undergo the nucleophilic attack by the alcohol, the steric hindrance of 2-ethylhexanoate groups is greater than that of the stearate groups. The reactivity of  $In(EH)_3$  matches that of  $Zn(St)_2$ , thereby achieving a more balanced reactivity of the cationic precursors. Furthermore,  $In(EH)_3$  is stable and does not undergo hydrolysis reactions when the temperature reaches as high as 220 °C (Figure 1c). FTIR analyses on the reverse-

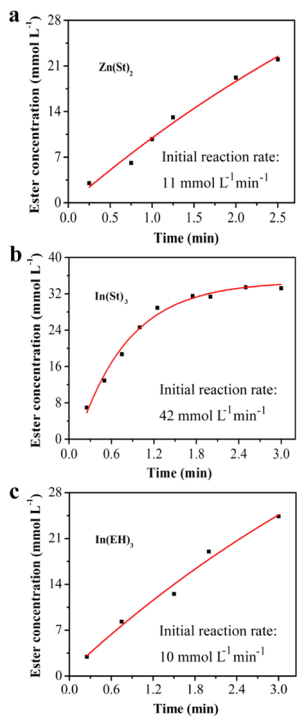


**Figure 2.** Initial ester-formation rates of the reverse-injection reactions for different cationic precursors. Reaction conditions:  $\text{Zn(St)}_2$  0.6 mmol/ $\text{In(EH)}_3$  0.4 mmol/ $\text{In(St)}_3$  0.4 mmol, ODA (6 mmol), ODE (16.5 g), and temperature = 250 °C. For all reactions, the flasks containing the metal precursors were carefully degassed and then kept at low temperatures ( $\text{In(St)}_3$ , 120 °C;  $\text{Zn(St)}_2$  and  $\text{In(EH)}_3$ , 150 °C) before the injection into the reaction flasks.

injection synthesis of IZO nanocrystals by using  $\text{In(EH)}_3$  and  $\text{Zn(St)}_2$  as precursors (Figure 3) or pure  $\text{In}_2\text{O}_3$  nanocrystals by using  $\text{In(EH)}_3$  as the precursor (see Figure S4 in the Supporting Information) indicated that no free acids were generated, demonstrating the controlled alcoholysis reaction pathways of  $\text{In(EH)}_3$ .

In short, the combination of employing the reverse-injection approach and using  $\text{Zn(St)}_2$  and  $\text{In(EH)}_3$  as the cationic precursors ensures both controlled reaction pathways and balanced dopant-host precursor reactivity. As to be discussed below, these concerted efforts lead to successful syntheses of high-quality colloidal IZO nanocrystals.

We emphasize that balancing the reactivity of the cationic precursors is critical for the synthesis of IZO nanocrystals. For

example, we conducted experiments using  $\text{In(EH)}_3$  and  $\text{Zn(EH)}_2$  as the precursors. In the reverse-injection synthesis, both  $\text{In(EH)}_3$  and  $\text{Zn(EH)}_2$  are stable and do not undergo hydrolysis reactions. However, the reactivity of  $\text{Zn(EH)}_2$  is too low to match that of  $\text{In(EH)}_3$ . As shown in Figure S5 in the Supporting Information, the initial ester formation rate for the reaction starting with 0.6 mmol of  $\text{Zn(EH)}_2$  is 0.64 mmol  $\text{L}^{-1} \text{min}^{-1}$ , more than 1 order of magnitude lower than that for the reaction starting with 0.4 mmol of  $\text{In(EH)}_3$ . The large difference in the reactivity of cationic precursors causes the failure of synthesizing phase-pure IZO nanocrystals (see Figure S6 in the Supporting Information).

The above experiments highlight the importance of selecting cationic precursors with suitable reactivity. We find that the empirical rule of relative Lewis acidity, which was used to guide the selections of precursors for several syntheses of ternary nanocrystals,<sup>25,54,55</sup> fails to predict the relative precursor reactivity in the case of alcoholysis of metal carboxylate salts. For instance,  $\text{St}^-$  is a hard coordinating ligand and both  $\text{In}^{3+}$  and  $\text{Mg}^{2+}$  ions are harder Lewis acids than  $\text{Zn}^{2+}$ . However, the quantitative measurements in this study show that  $\text{In(St)}_3$  is much more reactive than  $\text{Zn(St)}_2$  while our previous study<sup>53</sup> show that  $\text{Zn(St)}_2$  is more reactive than  $\text{Mg(St)}_2$ . We suggest that the rule of relative Lewis acidity is a suitable indicator to interpret the strengths of metal–ligand bonds. Other factors, such as interactions between the alkyl chains of the ligands, sizes of the cationic ions and lengths and structures of the coordination carboxylate ions may also play important roles in determining the reactivity of the carboxylate salts. In this regard, our method<sup>53</sup> to quantitatively study the chemical kinetics of alcoholysis reactions is highly desirable and critical for the selection of the host and dopant precursors in a rational manner.

**Controlled Doping of Colloidal IZO Nanocrystals.** The doped oxide nanocrystals from the reactions starting with 10 mol % of indium precursor, i.e.  $[\text{In(EH)}_3]/([\text{In(EH)}_3]+[\text{Zn(St)}_2])$  is 0.1, are used as an example to demonstrate the successful incorporation of indium dopants into  $\text{ZnO}$  lattices. The samples were characterized by a number of techniques, revealing the structural and chemical properties of the IZO nanocrystals. X-ray diffraction (XRD) profile of the doped oxide nanocrystals (Figure 4a) matches the hexagonal structure of wurtzite-type  $\text{ZnO}$  (JCPDS: 36–1451). Transmission electron microscopy (TEM) analyses show that the IZO nanocrystals, exhibiting decent monodispersity, are  $10.7 \pm 1.0$  nm in diameter. Energy-dispersive X-ray spectroscopy (EDS) analyses indicate the presence of indium (see Figure S7 in the Supporting Information). The EDS results agree with the inductively coupled plasma atomic emission spectroscopy (ICP-AES) measurements showing that the molar ratio of indium dopants, i.e.  $[\text{In}^{3+}]/([\text{Zn}^{2+}]+[\text{In}^{3+}])$ , is 14.6 at %. High resolution transmission electron microscopy (HRTEM) observations reveal the single-crystalline nature of the oxide nanocrystals. As shown in Figure 4c, the well-resolved lattice fringes with interplanar spacing of 0.283 nm correspond to the (100) lattice planes of wurtzite-type  $\text{ZnO}$ . We analyzed 201 HRTEM images with clear lattice fringes (see Figure S8 in the Supporting Information). No nanocrystals having crystal structure similar to that of corundum-type  $\text{In}_2\text{O}_3$  were found. Selected-area electron diffraction (SAED) characterization (see Figure S9 in the Supporting Information) shows that the diffraction pattern matches the structure of wurtzite-type  $\text{ZnO}$ , in line with the XRD and HRTEM results. In order to visualize

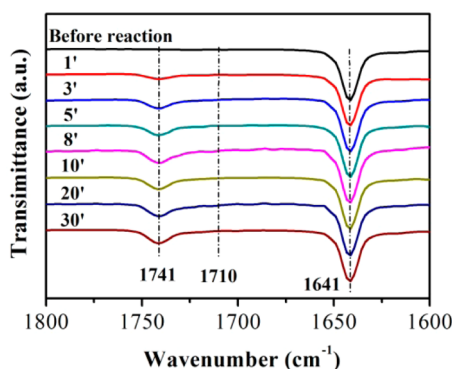


**Figure 3.** Temporal evolution of FTIR spectra recorded for a 10 mol %  $\text{In(EH)}_3$  reaction.

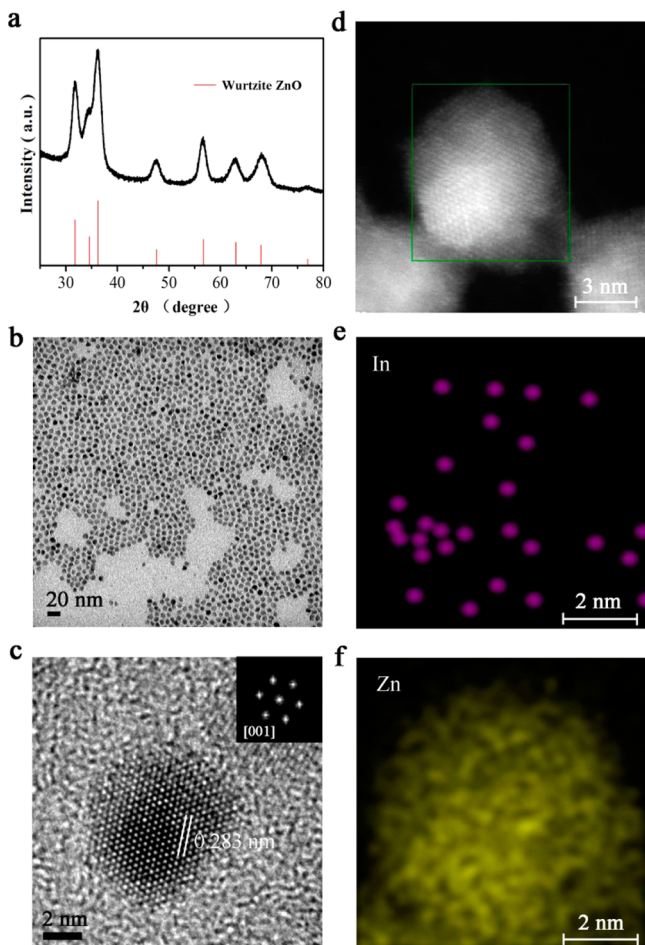


**Figure 4.** Structural and chemical properties of the IZO nanocrystals from the 10 mol %  $\text{In}(\text{EH})_3$  reactions. (a) XRD pattern. (b) Typical TEM image and (c) typical HRTEM image oriented along the [001] zone axis and the corresponding fast Fourier transform (FFT) pattern shown in the inset. The interplanar spacing of 0.283 nm corresponds to the (100) lattice plane of the wurtzite-type ZnO. (d) HAADF image for a single IZO nanocrystal and (e, f) corresponding EDS mapping of indium and zinc elements, respectively.

the distributions of indium ions in the oxide nanocrystals, high-angle annular dark-field (HAADF) experiments along with EDS mapping were carried out in an aberration-corrected scanning transmission electron microscope (STEM). The results shown in Figure 4d–f indicate randomly distributed indium dopant ions in one nanocrystal, agreeing with the XRD and HRTEM results of no segregation of dopant nanophasess. These characterizations provide solid evidence for the successful incorporation of indium dopants into host ZnO lattices.

The successful indium doping can also be assessed from optical measurements. As shown in Figure 5a, the ultraviolet-visible absorbance (UV-vis) spectrum of the IZO nanocrystals is different from that of the pure ZnO nanocrystals. The optical bandgaps of the oxide nanocrystals were determined from the derivative of the UV-vis absorption spectra.<sup>56</sup> The optical bandgap of the IZO nanocrystals, 3.44 eV, is greater than that of pure ZnO nanocrystals, 3.35 eV. We attribute the blue-shift of optical bandgaps to the Burstein–Moss effect. In other words, indium doping introduces a high density of free electrons, which populate the states close to the conduction band. Therefore, the IZO nanocrystals exhibit a larger optical

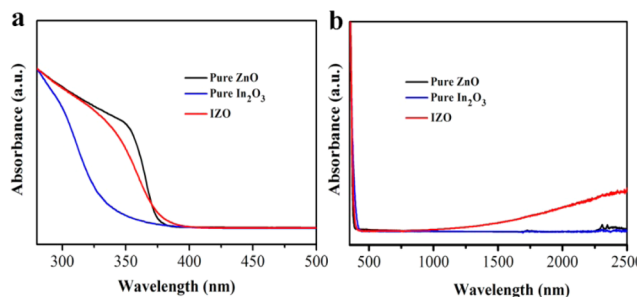


**Figure 5.** Optical properties of the IZO nanocrystals from the 10 mol %  $\text{In}(\text{EH})_3$  reaction. (a) UV–vis and (b) Vis–NIR spectra. The spectra of the pure ZnO and  $\text{In}_2\text{O}_3$  nanocrystals are also shown. The UV–vis spectra are normalized to the absorbance at 280 nm. The Vis–NIR spectra are normalized at the absorbance at 350 nm.

bandgap. The high density of free electrons in the IZO nanocrystals is confirmed by the characteristic surface plasmon resonance (SPR) peak in the near-infrared (NIR) region (Figure 5b), which is absent in the spectrum of pure ZnO nanocrystal samples.

Next we discuss the effects of molar ratio of  $\text{In}(\text{EH})_3$  in the reagents on the properties of IZO nanocrystals. A set of reactions starting with 0–20 mol % of  $\text{In}(\text{EH})_3$  were carried out. HRTEM characterizations on 187 individual nanocrystals from the 20 mol %  $\text{In}(\text{EH})_3$  reactions show that all the particles exhibit hexagonal structure of wurtzite-type ZnO (see Figure S10 in the Supporting Information), in agreement with the XRD profile that no reflection peaks from corundum-type  $\text{In}_2\text{O}_3$  (JCPDS: 06–0416) are observed (see Figure S11 in the Supporting Information). Therefore, the information from the following characterizations is associated with the properties of IZO nanocrystals with different doping concentrations. ICP-AES analyses indicate that the greater the molar ratio of  $\text{In}(\text{EH})_3$  in the starting materials, the higher the dopant concentration in the oxide nanocrystals (Figure 6a). In contrast, the optical bandgaps of the IZO nanocrystals extracted from the corresponding UV–vis spectra (see Figure S12 in the Supporting Information) and the molar ratios of  $\text{In}(\text{EH})_3$  in the reagents do not follow a monotonic increasing relationship (Figure 6b). We note that the optical bandgaps of IZO nanocrystals may be influenced by both the Burstein–Moss effect and size-dependent quantum confinement effect. Figure S13a–k in the Supporting Information shows the TEM images of the oxide nanocrystals from the reactions starting with different molar ratios of  $\text{In}(\text{EH})_3$ . The average diameters of all the nanocrystal samples are in the range of 8–11 nm (see Figure S13 in the Supporting Information), which is much larger than exciton Bohr radius of bulk ZnO nanocrystal, 1.8 nm. Our previous report shows that for pure ZnO nanocrystals, the optical bandgaps may be influenced by quantum confinement effects only when the sizes are smaller than 7 nm.<sup>28</sup> Therefore, we conclude that for our IZO samples, the changes on the optical bandgaps are due to Burstein–Moss effect. Figure 6b shows that the values of optical bandgap reach a maximum of 3.48 eV for the IZO nanocrystals from the 2.0 mol %  $\text{In}(\text{EH})_3$  reactions and then start to decrease when the indium dopant concentrations are higher. The SPR characteristics of the IZO nanocrystals were also examined (see Figure S14 in the Supporting Information). Figure 6c plots the intensities of SPR peaks at 2500 nm against the molar ratios of  $\text{In}(\text{EH})_3$  in the reagents. The trend is similar to that for the

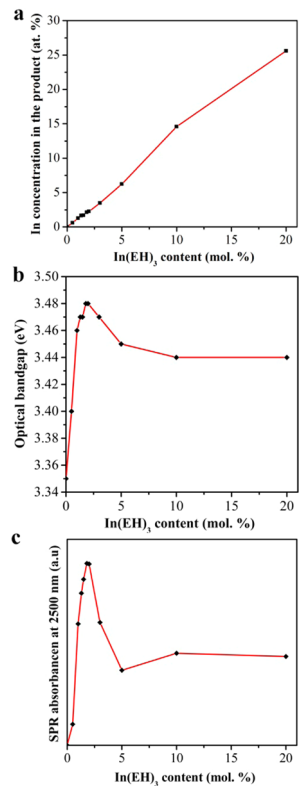


**Figure 6.** Effects of the molar ratios of In(EH)<sub>3</sub> in the reagents on the properties of the IZO nanocrystals. (a) Indium dopant concentrations determined by ICP-AES. (b) Optical bandgaps extracted from the spectra shown in Figure S12 in the Supporting Information. (c) SPR absorbance at 2500 nm of the IZO nanocrystals extracted from the spectra shown in Figure S14 in the Supporting Information, which are normalized to the absorbance at 350 nm.

optical bandgaps. These results suggest that IZO nanocrystals with the highest free-carrier density are obtained from the 2.0 mol % In(EH)<sub>3</sub> reactions, which correspond to a doping concentration of ~2.3 at %. Note that similar phenomena are also observed in a range of vapor deposited transparent conductive oxide thin-film systems (see Table S1 in the Supporting Information).<sup>57–75</sup> A defect model proposed by Köstlin et al. may be applied to explain this phenomenon.<sup>75</sup> Briefly, at a low doping level the higher the dopant concentration the higher the free carrier density because of the ionization of dopant impurities while in a highly doped system the neutral complexes of neighbor dopant cation-oxygen may form, leading to inactive dopants and decreased free carrier concentrations.

**IZO Nanocrystal Thin Films with Tunable Work Function.** Following the successful synthesis of colloidal IZO nanocrystals, we investigate the doping effects on the work function of oxide nanocrystal thin films.

Ligand exchange<sup>76</sup> is essential to applying the IZO nanocrystals in optoelectronic applications. Colloidal oxide nanocrystals synthesized by alcoholysis of metal fatty acid salts are generally capped by carboxylate ions with long alkyl-chains.<sup>27,51</sup> These bulky ligands act as insulating barriers, blocking charge transport between neighboring particles. Therefore, we used hexylamine to replace the original long-chain carboxylate ligands. The IZO nanocrystals from the 10 mol % In(EH)<sub>3</sub> reactions are used as an example to study the ligand-exchange processes. Figure 7a shows the FTIR spectra of

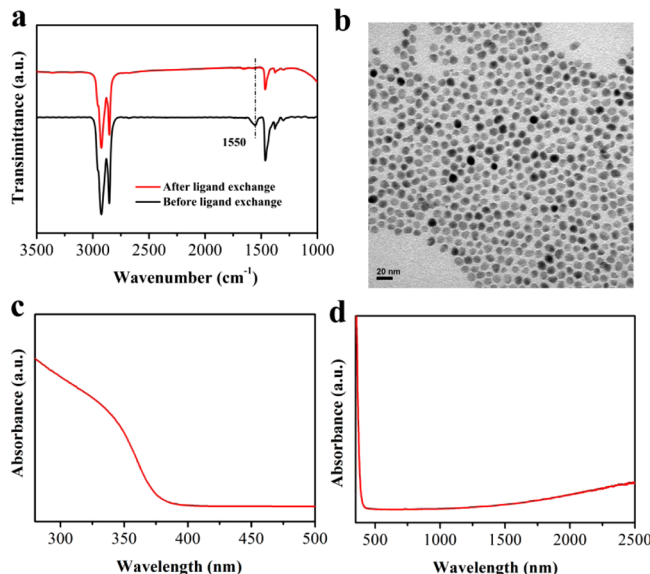


**Figure 7.** Ligand exchange on the IZO nanocrystals from the 10 mol % In(EH)<sub>3</sub> reactions. (a) FTIR spectra. (b) Typical TEM image, (c) UV-vis, and (d) Vis-NIR spectra of the ligand-exchanged IZO nanocrystals.

IZO nanocrystals. The peak at 1550 cm<sup>-1</sup> corresponding to the asymmetric vibration of carboxylate groups disappears after the experiment, indicating that the proposed ligand exchange is effective. TEM analyses (Figure 7b) show that the diameters of the ligand-exchanged IZO nanocrystals are  $10.5 \pm 0.9$  nm, similar to that of the nanocrystals before ligand exchange. The indium concentration, 14.3 at %, and the optical bandgap extracted from the UV-vis spectrum (Figure 7c), 3.43 eV, of the IZO nanocrystals after ligand exchange is close to those of the oxide nanocrystals before ligand exchange. As shown in Figure 7d, the ligand-exchanged IZO nanocrystals exhibit characteristic SPR absorbance in the NIR region. These results demonstrate that the successful indium doping into the oxide nanocrystals is preserved after the ligand exchange processes.

Oxide films were prepared by spin coating the nanocrystals onto substrates, followed by mild annealing at 140 °C for 40 min in a nitrogen-filled glovebox. Figure S15 in the Supporting Information shows the UV-vis-NIR spectra of IZO nanocrystal thin films deposited onto quartz substrates. The spectrum of the film without annealing is identical to that of the same film after annealing. This result indicates that the low-temperature (140 °C) annealing procedure in a glovebox does not change the free carrier density of the IZO nanocrystal films.

The work function of thin films based on ligand-exchanged oxide nanocrystals is measured by ultraviolet photoelectron spectroscopy (UPS). All samples were deposited onto ITO-glass substrates. Figure S16 in the Supporting Information shows the top-views of oxide nanocrystal thin films based on pure ZnO nanocrystals and IZO nanocrystals from the 2 mol % In(EH)<sub>3</sub> reaction, demonstrating uniform and pinhole free surface features. The work function of the thin films is obtained from the secondary electron cut-offs (Figure 8a and Figure S17 in the Supporting Information). Five samples based on oxide nanocrystals from reaction starting with different molar ratio of In(EH)<sub>3</sub> were characterized. The values are plotted in Figure 8b. The work function of thin films based on pure ZnO nanocrystals and the IZO nanocrystals from the 2.0 mol %

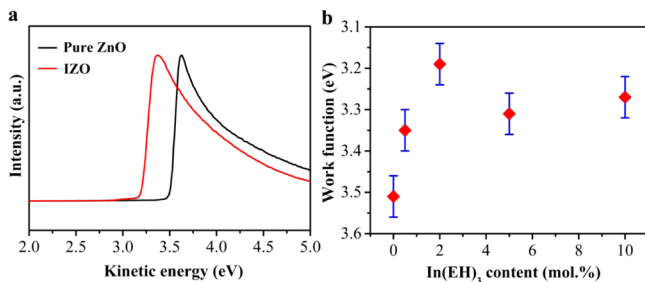


**Figure 8.** Work function of thin films based on oxide nanocrystals. (a) UPS spectra showing the normalized secondary electron cutoff. The IZO nanocrystals to prepare this sample is from the 2 mol % In(EH)<sub>3</sub> reaction. The UPS spectra for the films based on oxide nanocrystals from 0.5, 5, and 10 mol % In(EH)<sub>3</sub> reactions are shown in Figure S17 in the Supporting Information. (b) Work function of five samples from reactions starting with 0, 0.5, 2, 5, and 10 mol % In(EH)<sub>3</sub> reactions. The error bar of  $\pm 0.05$  eV comes from the overall accuracy of the instrument.

In(EH)<sub>3</sub> reaction is 3.5 and 3.2 eV, respectively, giving the maximum difference of 0.3 eV in the five samples.

We suggest that the variations in work function can be mainly attributed to the different free electron concentrations of the oxide nanocrystal films. The higher the free electron concentration, the lower the work function of the oxide nanocrystal films. In other words, controlled doping leads to oxide nanocrystals with different free electron concentrations and hence oxide nanocrystal thin films with tunable work function (Figure 8b). Given that identical synthetic and processing procedures were used to obtain the UPS samples, surface dipole is unlikely to contribute to the work-function differences. This is supported by our UPS data that the difference in the energy levels of valence band maximum (relative to the vacuum level) for the films based on pure ZnO nanocrystals and IZO nanocrystals from the 2.0 mol % In(EH)<sub>3</sub> reaction is within 0.1 eV. Therefore, the variation of the Fermi level is mainly due to the filling of free electrons into the conduction band. We further estimated this effect in bulk ZnO by assuming ZnO is heavily doped and can be treated as a degenerated semiconductor (see Figure S18 in the Supporting Information). The calculation shows that when the free electron concentration changes from  $2.5 \times 10^{18}$  to  $9.8 \times 10^{19}$  cm<sup>-3</sup>, the Fermi level moves toward the vacuum level by 0.3 eV from the energy level of conduction band minimum.

**IZO Nanocrystal Thin Films as ETLs in PLEDs.** The oxide nanocrystal thin films were applied in PLEDs to study the effects of work function of oxide nanocrystal ETLs on the device performances. We select pure ZnO nanocrystals and the IZO nanocrystals from the 2.0 mol % In(EH)<sub>3</sub> reactions because thin films based on these two kinds of oxide nanocrystals exhibit the largest work-function difference. Figure 9a shows that both oxide nanocrystal thin film coated ITO substrates are highly transparent in the visible region with an average transmittance over 83% from 400 to 800 nm. The atomic force microscopy (AFM) images shown in Figure 9b, c reveal that both oxide nanocrystal thin films exhibit flat surface features with root-mean-square roughness of ~2.9 nm. The excellent optical transparency and flat surface features suggest that the oxide nanocrystal thin films are suitable for ETL applications.

A device structure of ITO/oxide nanocrystal ETL/F8BT/MoO<sub>3</sub>/Al is used to fabricate PLEDs (Figure 10a). The

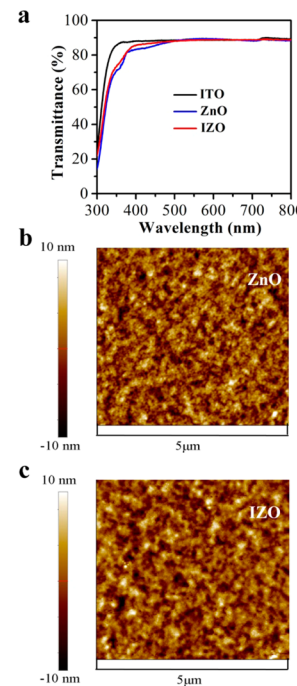


**Figure 9.** Oxide nanocrystal thin films. (a) Optical transmittance spectra. The spectrum for the ITO-glass substrate is also shown. (b, c) AFM images for the ZnO and IZO nanocrystal thin films, respectively. The IZO nanocrystals from the 2 mol % In(EH)<sub>3</sub> reactions were used.

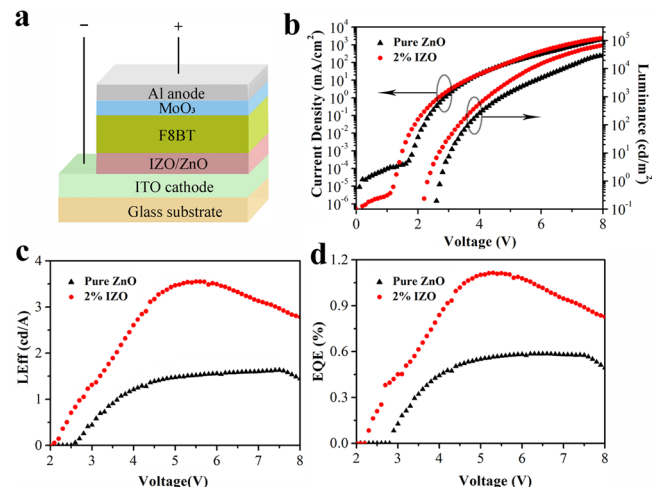


**Figure 10.** PLEDs with oxide nanocrystal ETLs. (a) Device structure. (b)  $J$ – $L$ – $V$  curves, (c) current efficiency– $V$  curves, and (d) EQE– $V$  curves. The IZO nanocrystals from the 2 mol % In(EH)<sub>3</sub> reactions were used.

characteristics of two devices (one device with IZO ETLs and another control device with ZnO ETLs), including current density ( $J$ )–luminance ( $L$ )–voltage( $V$ ) curves, current efficiency– $V$  curves and external quantum efficiency (EQE)– $V$  curves, are shown in Figure 10b, 10c and 10d, respectively. The statistical on the parameters from 25 devices for each type of PLED are shown in Figure S19 in the Supporting Information. Averagely, the PLEDs with IZO nanocrystal ETLs exhibit a turn-on voltage (the voltage corresponds to a luminance of 1 cd m<sup>-2</sup>) of 2.2 V, a maximum brightness of over 78,000 cd m<sup>-2</sup> at 8 V, a maximum EQE of 1.0% and a maximum current efficiency of 3.2 cd A<sup>-1</sup>, respectively. Figure 10b–d and Figure

S19 in the Supporting Information also demonstrate that the devices with IZO nanocrystal ETLs exhibit significantly better performances in terms of lower turn-on voltages, higher maximum luminance and higher efficiency, compared with the devices with ZnO nanocrystal ETLs.

We attribute the better device performances to the improved electron-injection characteristics induced by the lower work function of the IZO nanocrystal ETLs. This correlation is supported by scanning Kelvin probe microscopy (SKPM) investigations on the bilayers of F8BT/oxide nanocrystal thin films (Figure 11a).<sup>77</sup> As depicted in Figure 11, the surface potential profiles of the bilayer films reflect the difference in work function at the interface of the contacting F8BT and oxide nanocrystal layers. The surface potential of the ZnO nano-

crystal area is about 50 meV more negative than that of the F8BT area, while the surface potential of the IZO nanocrystal area is more positive than that of the F8BT area. These results suggest that for the ETLs based on the ZnO nanocrystals, there is a moderate energy barrier for electron injection. In contrast, due to the doping effects, the ETLs based on IZO nanocrystals have lower work function and thereby there should be no electron injection barrier for electron injection into the F8BT emitting layers.

## CONCLUSIONS

We demonstrate that rational synthesis of colloidal IZO nanocrystals leads to controlled indium doping into the ZnO lattices, which lowers the work function of the oxide nanocrystal thin films. Mechanism studies on the precursor conversion reactions reveal that controlling the reaction pathways and the balancing relative reactivity of cationic precursors are critical in terms of achieving high quality doped oxide nanocrystals. The colloidal IZO nanocrystals were characterized by a number of techniques, demonstrating that successful incorporation of indium dopants into oxide nanocrystals leads to high free-carrier density. ETLs based on IZO nanocrystals exhibit lower work function and improved electron-injection characteristics, enhancing the performances of the PLEDs with F8BT emitters. Our study is an excellent example that new understanding on the chemical kinetics of doped nanocrystals leads to rational design of synthetic protocols and materials with tailored electronic properties, providing benefits for their optoelectronic applications.

## ASSOCIATED CONTENT

### Supporting Information

Characterization techniques, syntheses of indium precursors, additional figures and tables. This material is available free of charge via the Internet at <http://pubs.acs.org>.

## AUTHOR INFORMATION

### Corresponding Author

\*E-mail: [yizhengjin@zju.edu.cn](mailto:yizhengjin@zju.edu.cn).

### Notes

The authors declare no competing financial interest.

## ACKNOWLEDGMENTS

This work is financially supported by the National High Technology Research and Development Program of China (2011AA050520), the National Basic Research Program of China (2014CB932500), the National Natural Science Foundation of China (51172203, 51222202), the Natural Science Funds for Distinguished Young Scholar of Zhejiang Province (R4110189), the Public Welfare Project of Zhejiang Province (2013C31057), the fundamental Research Funds for the Central Universities (2014XZZX003-07) and the Program for Innovative Research Team in University of Ministry of Education of China (IRT13037). The work on TEM was done in Center of Electron Microscopy of Zhejiang University. We thank Prof. Xiaogang Peng (Zhejiang University, China) for the valuable discussions.

## REFERENCES

- (1) Graetzel, M.; Janssen, R. A. J.; Mitzi, D. B.; Sargent, E. H. *Nature* **2012**, *488*, 304–312.

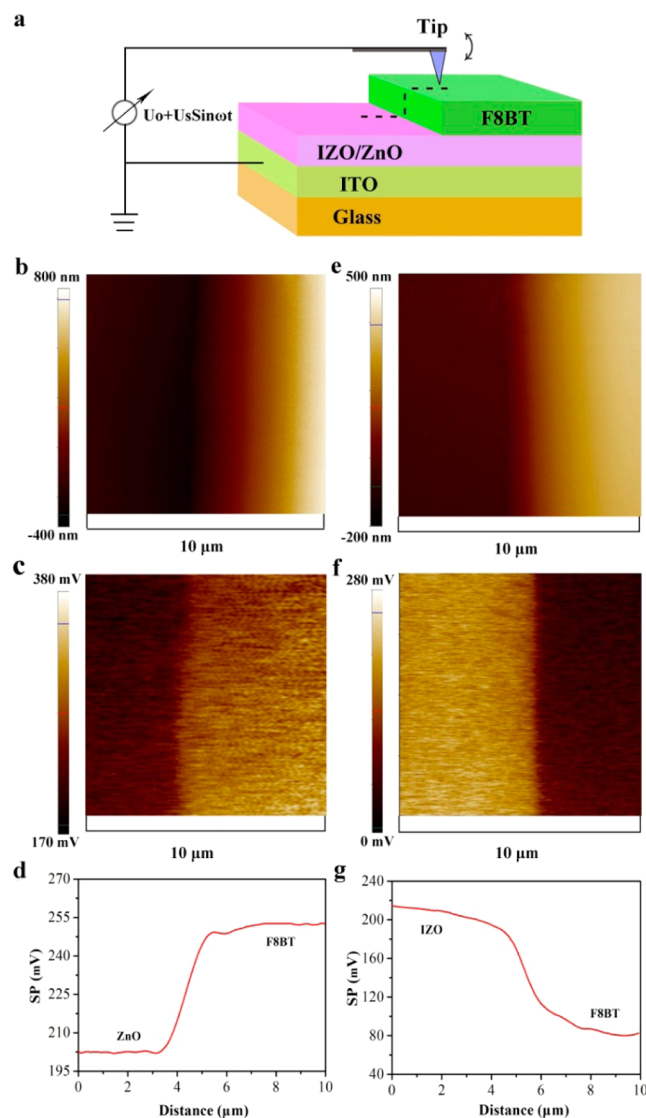


**Figure 11.** SKPM measurements on the bilayers of oxide ETLs/F8BT. (a) Schematic illustration of the experimental setup. (b) Topographic image, (c) corresponding surface potential image, and (d) smoothed cross-sectional line profile of the surface potential image in c for the ZnO nanocrystal thin films partially covered by F8BT. (e) Topographic image, (f) corresponding surface potential image, and (g) smoothed cross-sectional line profile of the surface potential image in f for the IZO nanocrystal thin films partially covered by F8BT. The IZO nanocrystals from the 2 mol %  $\text{In}(\text{EH})_3$  reactions were used.

- (2) Friend, R. H.; Gymer, R. W.; Holmes, A. B.; Burroughes, J. H.; Marks, R. N.; Taliani, C.; Bradley, D. D. C.; Santos, D. A. D.; Bredas, J. L.; Logdlund, M.; et al. *Nature* **1999**, *397*, 121–128.
- (3) Stranks, S. D.; Eperon, G. E.; Grancini, G.; Menelaou, C.; Alcocer, M. J. P.; Leijtens, T.; Herz, L. M.; Petrozza, A.; Snaith, H. J. *Science* **2013**, *342*, 341–344.
- (4) Talapin, D. V.; Lee, J.-S.; Kovalenko, M. V.; Shevchenko, E. V. *Chem. Rev.* **2009**, *110*, 389–458.
- (5) Konstantatos, G.; Howard, I.; Fischer, A.; Hoogland, S.; Clifford, J.; Klem, E.; Levina, L.; Sargent, E. H. *Nature* **2006**, *442*, 180–183.
- (6) Jin, Y. Z.; Wang, J. P.; Sun, B. Q.; Blakesley, J. C.; Greenham, N. C. *Nano Lett.* **2008**, *8*, 1649–1653.
- (7) Sun, B. Q.; Sirringhaus, H. *Nano Lett.* **2005**, *5*, 2408–2413.
- (8) Shirasaki, Y.; Supran, G. J.; Bawendi, M. G.; Bulovic, V. *Nat. Photonics* **2013**, *7*, 13–23.
- (9) Luther, J. M.; Law, M.; Beard, M. C.; Song, Q.; Reese, M. O.; Ellingson, R. J.; Nozik, A. J. *Nano Lett.* **2008**, *8*, 3488–3492.
- (10) Waldauf, C.; Morana, M.; Denk, P.; Schilinsky, P.; Coakley, K.; Choulis, S. A.; Brabec, C. J. *Appl. Phys. Lett.* **2006**, *89*, 233517–3.
- (11) Sun, Y. M.; Seo, J. H.; Takacs, C. J.; Seifert, J.; Heeger, A. J. *Adv. Mater.* **2011**, *23*, 1679–1683.
- (12) Sun, Y. M.; Takacs, C. J.; Cowan, S. R.; Seo, J. H.; Gong, X.; Roy, A.; Heeger, A. J. *Adv. Mater.* **2011**, *23*, 2226–2230.
- (13) Meyer, J.; Hamwi, S.; Kröger, M.; Kowalsky, W.; Riedl, T.; Kahn, A. *Adv. Mater.* **2012**, *24*, 5408–5427.
- (14) Bai, S.; Cao, M. T.; Jin, Y. Z.; Dai, X. L.; Liang, X. Y.; Ye, Z. Z.; Li, M.; Cheng, J. P.; Xiao, X. Z.; Wu, Z. W. *Adv. Energy Mater.* **2014**, *4*, No. 1301460.
- (15) Bai, S.; Wu, Z. W.; Xu, X. L.; Jin, Y. Z.; Sun, B. Q.; Guo, X. J.; He, S. S.; Wang, X.; Ye, Z. Z.; Wei, X. H.; et al. *Appl. Phys. Lett.* **2012**, *100*, 203906.
- (16) Chen, S.; Manders, J. R.; Tsang, S.-W.; So, F. J. *Mater. Chem.* **2012**, *22*, 24202–24212.
- (17) Greiner, M. T.; Lu, Z.-H. *NPG Asia Mater.* **2013**, *5*, e55.
- (18) Greiner, M. T.; Helander, M. G.; Tang, W.-M.; Wang, Z.-B.; Qiu, J.; Lu, Z.-H. *Nat. Mater.* **2012**, *11*, 76–81.
- (19) Ratcliff, E. L.; Garcia, A.; Paniagua, S. A.; Cowan, S. R.; Giordano, A. J.; Ginley, D. S.; Marder, S. R.; Berry, J. J.; Olson, D. C. *Adv. Energy Mater.* **2013**, *3*, 647–656.
- (20) Meyer, J.; Khalandovsky, R.; Görrn, P.; Kahn, A. *Adv. Mater.* **2011**, *23*, 70–73.
- (21) You, J. B.; Chen, C.-C.; Dou, L. T.; Murase, S.; Duan, H. S.; Hawks, S. A.; Xu, T.; Son, H. J.; Yu, L. P.; Li, G.; et al. *Adv. Mater.* **2012**, *24*, 5267–5272.
- (22) Hau, S. K.; Yip, H.-L.; Baek, N. S.; Zou, J.; O’Malley, K.; Jen, A. K. Y. *Appl. Phys. Lett.* **2008**, *92*, 253301–3.
- (23) Lee, Y.-J.; Yi, J.; Gao, G. F.; Koerner, H.; Park, K.; Wang, J.; Luo, K. Y.; Vaia, R. A.; Hsu, J. W. P. *Adv. Energy Mater.* **2012**, *2*, 1193–1197.
- (24) Liang, X. Y.; Yi, Q.; Bai, S.; Dai, X. L.; Wang, X.; Ye, Z. Z.; Gao, F.; Zhang, F. L.; Sun, B. Q.; Jin, Y. Z. *Nano Lett.* **2014**, *14*, 3117–3123.
- (25) Buonsanti, R.; Llordes, A.; Aloni, S.; Helms, B. A.; Milliron, D. J. *Nano Lett.* **2011**, *11*, 4706–4710.
- (26) Cohn, A. W.; Kittilstved, K. R.; Gamelin, D. R. *J. Am. Chem. Soc.* **2012**, *134*, 7937–7943.
- (27) Yang, Y. F.; Jin, Y. Z.; He, H. P.; Wang, Q. L.; Tu, Y.; Lu, H. M.; Ye, Z. Z. *J. Am. Chem. Soc.* **2010**, *132*, 13381–13394.
- (28) Wang, X.; Jin, Y. Z.; He, H. P.; Yang, F.; Yang, Y. F.; Ye, Z. Z. *Nanoscale* **2013**, *5*, 6464–6468.
- (29) Ghosh, S.; Saha, M.; De, S. K. *Nanoscale* **2014**, *6*, 7039–7051.
- (30) Ishii, H.; Sugiyama, K.; Ito, E.; Seki, K. *Adv. Mater.* **1999**, *11*, 605–625.
- (31) Ma, H.; Yip, H.-L.; Huang, F.; Jen, A. K. -Y. *Adv. Funct. Mater.* **2010**, *20*, 1371–1388.
- (32) Greiner, M. T.; Chai, L.; Helander, M. G.; Tang, W.-M.; Lu, Z.-H. *Adv. Funct. Mater.* **2012**, *22*, 4557–4568.
- (33) Kanehara, M.; Koike, H.; Yoshinaga, T.; Teranishi, T. *J. Am. Chem. Soc.* **2009**, *131*, 17736–17737.
- (34) Della Gaspera, E.; Bersani, M.; Cittadini, M.; Guglielmi, M.; Pagani, D.; Noriega, R.; Mehra, S.; Salleo, A.; Martucci, A. *J. Am. Chem. Soc.* **2013**, *135*, 3439–3448.
- (35) De Trizio, L.; Buonsanti, R.; Schimpf, A. M.; Llordes, A.; Gamelin, D. R.; Simonutti, R.; Milliron, D. J. *Chem. Mater.* **2013**, *25*, 3383–3390.
- (36) Xie, R. G.; Li, Z.; Peng, X. G. *J. Am. Chem. Soc.* **2009**, *131*, 15457–15466.
- (37) Liu, H. T.; Owen, J. S.; Alivisatos, A. P. *J. Am. Chem. Soc.* **2007**, *129*, 305–312.
- (38) Owen, J. S.; Chan, E. M.; Liu, H. T.; Alivisatos, A. P. *J. Am. Chem. Soc.* **2010**, *132*, 18206–18213.
- (39) Li, Z.; Ji, Y. J.; Xie, R. G.; Grisham, S. Y.; Peng, X. G. *J. Am. Chem. Soc.* **2011**, *133*, 17248–17256.
- (40) Abe, S.; Čapek, R. K.; De Geyter, B.; Hens, Z. *ACS Nano* **2011**, *6*, 42–53.
- (41) Hendricks, M. P.; Cossairt, B. M.; Owen, J. S. *ACS Nano* **2012**, *6*, 10054–10062.
- (42) Wang, F. D.; Buhro, W. E. *J. Am. Chem. Soc.* **2012**, *134*, 5369–5380.
- (43) Chen, D. A.; Viswanatha, R.; Ong, G. L.; Xie, R. G.; Balasubramanian, M.; Peng, X. G. *J. Am. Chem. Soc.* **2009**, *131*, 9333–9339.
- (44) Karan, N. S.; Sarkar, S.; Sarma, D. D.; Kundu, P.; Ravishankar, N.; Pradhan, N. *J. Am. Chem. Soc.* **2011**, *133*, 1666–1669.
- (45) Erwin, S. C.; Zu, L. J.; Haftel, M. I.; Efros, A. L.; Kennedy, T. A.; Norris, D. J. *Nature* **2005**, *436*, 91–94.
- (46) Qian, L.; Zheng, Y.; Xue, J. G.; Holloway, P. H. *Nat. Photonics* **2011**, *5*, 543–548.
- (47) Qian, L.; Zheng, Y.; Choudhury, K. R.; Bera, D.; So, F.; Xue, J. G.; Holloway, P. H. *Nano Today* **2010**, *5*, 384–389.
- (48) Liu, D.; Kelly, T. L. *Nat. Photonics* **2014**, *8*, 133–138.
- (49) Wang, Q. L.; Yang, Y. F.; He, H. P.; Chen, D. D.; Ye, Z. Z.; Jin, Y. Z. *Nanoscale Res. Lett.* **2010**, *5*, 882–888.
- (50) Narayanaswamy, A.; Xu, H. F.; Pradhan, N.; Kim, M.; Peng, X. G. *J. Am. Chem. Soc.* **2006**, *128*, 10310–10319.
- (51) Chen, Y. F.; Kim, M.; Lian, G.; Johnson, M. B.; Peng, X. G. *J. Am. Chem. Soc.* **2005**, *127*, 13331–13337.
- (52) Jin, Y. Z.; Yi, Q.; Ren, Y. P.; Wang, X.; Ye, Z. Z. *Nanoscale Res. Lett.* **2013**, *8*, 153.
- (53) Zhang, N.; Wang, X.; Jin, Y. Z.; Ye, Z. Z. *Sci. Rep.* **2014**, *4*, 4353.
- (54) Buonsanti, R.; Milliron, D. J. *Chem. Mater.* **2013**, *25*, 1305–1317.
- (55) Xie, R. G.; Rutherford, M.; Peng, X. G. *J. Am. Chem. Soc.* **2009**, *131*, 5691–5697.
- (56) Srinivasan, S.; Bertram, F.; Bell, A.; Ponce, F. A.; Tanaka, S.; Omiya, H.; Nakagawa, Y. *Appl. Phys. Lett.* **2002**, *80*, 550–552.
- (57) Chalker, P. R.; Marshall, P. A.; Romani, S.; Roberts, J. W.; Irvine, S. J. C.; Lamb, D. A.; Clayton, A. J.; Williams, P. A. *J. Vac. Sci. Technol., A* **2013**, *31*, 01A120.
- (58) Deng, Z. H.; Huang, C. G.; Huang, J. Q.; Wang, M. L.; He, H.; Wang, H.; Cao, Y. G. *J. Mater. Sci.: Mater. Electron.* **2010**, *21*, 1030–1035.
- (59) Kim, W.-H.; Maeng, W. J.; Kim, M.-K.; Kim, H. *J. Electrochem. Soc.* **2011**, *158*, D495.
- (60) Lin, K.-m.; Chen, Y.-Y.; Chiu, C.-Y. *J. Sol-Gel Sci. Technol.* **2010**, *55*, 299–305.
- (61) Luka, G.; Krajewski, T. A.; Witkowski, B. S.; Wisz, G.; Virt, I. S.; Guziewicz, E.; Godlewski, M. *J. Mater. Sci.: Mater. Electron.* **2011**, *22*, 1810–1815.
- (62) Mridha, S.; Basak, D. *J. Phys. D: Appl. Phys.* **2007**, *40*, 6902–6907.
- (63) Salam, S.; Islam, M.; Akram, A. *Thin Solid Films* **2013**, *529*, 242–247.
- (64) Seo, S.-W.; Won, S. H.; Chae, H.; Cho, S. M. *Korean J. Chem. Eng.* **2012**, *29*, 525–528.
- (65) Singh, A. V. *J. Appl. Phys.* **2004**, *95*, 3640.
- (66) Yu, C.-F.; Chen, S.-H.; Sun, S.-J.; Chou, H. *Appl. Surf. Sci.* **2011**, *257*, 6498–6502.

- (67) Shind, S. S.; Shind, P. S.; Bhosale, C. H.; Rajpure, K. Y. *J. Phys. D: Appl. Phys.* **2008**, *41*, 105109.
- (68) Goyal, D. J.; Agashe, C.; Takwale, M. G.; Bhide, V. G. *J. Mater. Res.* **1993**, *8*, 1052–1056.
- (69) Maeng, W. J.; Lee, J. W.; Lee, J. H.; Chung, K. B.; Park, J. S. *J. Phys. D: Appl. Phys.* **2011**, *44* (44), 445305.
- (70) Ayadi, Z. B.; Mir, L. E.; Djessas, K.; Alaya, S. *Nanotechnology* **2007**, *18* (44), 445702.
- (71) Ye, J. D.; Gu, S. L.; Zhu, S. M.; Liu, S. M.; Zheng, Y. D.; Zhang, R.; Shi, Y.; Yu, H. Q.; Ye, Y. D. *J. Cryst. Growth* **2005**, *283*, 279–285.
- (72) Kim, H.; Pique, A.; Horwitz, J. S.; Murata, H.; Kafafi, Z. H.; Gilmore, C. M.; Chrisey, D. B. *Thin Solid Films* **2000**, *377*, 798–802.
- (73) Nunes, P.; Fortunato, E.; Tonello, P.; Fernandes, F. B.; Vilarinho, P.; Martins, R. *Vacuum* **2002**, *64*, 281–285.
- (74) Paul, G. K.; Sen, S. K. *Mater. Lett.* **2002**, *57*, 742–746.
- (75) Frank, G.; Köstlin, H. *Appl. Phys. A: Mater. Sci. Process.* **1982**, *27*, 197–206.
- (76) Luo, J.; Dai, X. I.; Bai, S.; Jin, Y. Z.; Ye, Z. Z.; Guo, X. J. *Nano-Micro Lett.* **2013**, *5*, 274–280.
- (77) He, Z. C.; Zhong, C. M.; Huang, X.; Wong, W. Y.; Wu, H. B.; Chen, L. W.; Su, S. J.; Cao, Y. *Adv. Mater.* **2011**, *23*, 4636–4643.